

# Impact of Model Resolution on the Representation of the Wind Field Along Nares Strait

G. W. K. Moore ([✉ gwk.moore@utoronto.ca](mailto:gwk.moore@utoronto.ca))

University of Toronto

---

## Research Article

**Keywords:** Nares Strait, wind field, model resolution, sea ice leaves

**Posted Date:** March 5th, 2021

**DOI:** <https://doi.org/10.21203/rs.3.rs-274613/v1>

**License:**  This work is licensed under a Creative Commons Attribution 4.0 International License.

[Read Full License](#)

---

## ***Impact of model resolution on the representation of the wind field along Nares Strait***

2

3

G. W. K. Moore<sup>1,2\*</sup>

5

<sup>1</sup> Department of Physics, University of Toronto, Toronto, Ontario, Canada

7

8

<sup>2</sup> Department of Chemical and Physical Sciences, University of Toronto Mississauga, Mississauga, Ontario, Canada

10

\*email: [gwk.moore@utoronto.ca](mailto:gwk.moore@utoronto.ca)

12

13

Manuscript to be submitted to *Scientific Reports*

14

February 25, 21

15

16

17

18     **Abstract**

19                 Nares Strait is a major pathway along which multi-year sea ice leaves the Arctic,  
20     an ice class that seen a recent dramatic reduction in extent. The winds that blow along the  
21     strait play an important role in modulating this ice export as well as in establishing the  
22     Arctic's largest and most productive polynya, the North Water, that forms at its southern  
23     terminus. However, its remote location has limited knowledge of the winds along the strait.  
24     Here we use automatic weather station from Hans Island, in the middle of the strait, to  
25     assess the ability of a set of atmospheric analyses with a common lineage but with varying  
26     horizontal resolution to represent the variability in the wind field. We find that the flow is  
27     highly bidirectional, consistent with topographic channeling, with the highest wind speeds  
28     from the north and that a model resolution of ~9km is required to capture the observed  
29     variability. The wind field at Hans Island is also found to be representative of variability  
30     in the flow along much of Nares Strait.

31     **Introduction**

32                 Nares Strait is the ~600km long strait that connects the Arctic Ocean's Lincoln Sea  
33     to northern Baffin Bay (Figure 1). The high topography along both sides of the strait  
34     (Figure 1) as well as the generally higher sea-level pressures over the Lincoln Sea as  
35     compared to northern Baffin Bay results in a tendency for northerly flow down the strait  
36     [Samelson *et al.*, 2006]. The oldest and thickest sea ice in the Arctic is situated to the north  
37     of Nares Strait [Moore *et al.*, 2019] and the strait is a major pathway for the export of this  
38     important ice class out of the Arctic [Kwok *et al.*, 2010]. The wind field along Nares Strait  
39     with its preference for northly flow plays a role in the export [Samelson *et al.*, 2006].

40       Ice arches that form most winters along Nares Strait, either in the vicinity of Smith  
41       Sound or the Robeson Channel- please refer to Figure 1 for place names in the region, can  
42       result in the cessation of ice transport for months at a time [Kwok *et al.*, 2010; Moore *et*  
43       *al.*, 2021]. The presence of these arches also contributes to the largest and most productive  
44       polynya in the Arctic, the North Water (NOW) that forms at the southern end of Nares  
45       Strait (Figure 1), in the vicinity of Smith Sound [Ingram *et al.*, 2002]. With an arch present,  
46       ice motion along the strait is inhibited and the northerly flow down Nares Strait that  
47       accelerates in the exit region of Smith Sound is able to remove any existing or new sea ice  
48       contributing to the maintenance of the polynya's open water [Barber *et al.*, 2001].

49       There is evidence that the ice bridges along Nares Strait are becoming less stable  
50       [Moore *et al.*, 2021] and that the area of the NOW is increasing [April *et al.*, 2019]. There  
51       is also evidence that anomalous winds play a role in the collapse of these arches [Moore  
52       and McNeil, 2018]. In addition, the Arctic is undergoing a transition towards a younger  
53       [Maslanik *et al.*, 2011] and thinner [Lindsay and Schweiger, 2015] ice pack that is leading  
54       to a loss of multi-year ice from the Arctic [Kwok, 2018]. There has also recently been an  
55       increase in both ice area and ice volume fluxes along Nares Strait [Moore *et al.*, 2021] that  
56       has been suggested to contribute to the Arctic's loss of multi-year ice [Kwok *et al.*, 2010].

57       The remote and data sparse nature of the region implies that there is still  
58       considerable uncertainty regarding the characteristics of the wind field that limits our  
59       ability to fully understand its role in ice export and its contribution to the formation of the  
60       NOW as well as the wind's role in the changes that are occurring in the region. Limited  
61       wind observations from the Smith Sound region confirm the preference for northerly flow  
62       with mean wind speeds on the order of 6-8 m s<sup>-1</sup> [Ingram *et al.*, 2002; Ito, 1982]. However

63 observations extending back to the 1860s indicate that long-lived gales, events  
64 characterized by northerly surface wind speeds in excess of  $20\text{ ms}^{-1}$ , are a common  
65 occurrence in the Smith Sound region during the winter months [Steffen, 1985].

66 Wind observations farther north along Nares Strait are even rarer. In April 2005, an  
67 ice camp established along the Kennedy Channel was destroyed by north winds in excess  
68 of  $25\text{ ms}^{-1}$  [Melling, 2011; Samelson and Barbour, 2008]. During the United States North  
69 Polar Expedition, the expedition's ship was trapped in ice at an exposed site in Hall Basin  
70 during the winter of 1871-72 and the science party regularly observed wind speeds in  
71 excess of  $20\text{ ms}^{-1}$  with a preference for northly flow [Bessels, 1876]. In the vicinity of  
72 Robeson Channel, meteorological observations were made at Fort Conger from August  
73 1881 to August 1883 during the First Polar Year by members of the United States  
74 Expedition to Lady Franklin Bay [Greely, 1888]. These observations indicated the  
75 preference for bidirectional wind flow, either in the NNE or SSW direction, along Robeson  
76 Channel. There were numerous events, with both directionalities, where the wind speeds  
77 were in excess of  $15\text{ m/s}$  [Greely, 1888].

78 Hans Island ( $80^{\circ}49'35''\text{N}$ ,  $66^{\circ}27'35''\text{W}$ ), jointly claimed by both Canada and  
79 Denmark, is situated in the middle of the Kennedy Channel, one of the narrower sections  
80 of Nares Strait (Figures 1 and 2). Since 2008, an automatic weather station (AWS) has  
81 been operating on this island [Wilkinson et al., 2009] with data currently available from  
82 2016 onwards.

83 In this paper, a sequence of reanalyses and an operational analysis with horizontal  
84 resolutions ranging from  $\sim 60\text{ km}$  to  $\sim 9\text{ km}$ , that all share a common heritage, to characterize  
85 the variability in the wind field as observed by this weather station. This approach, that

86 employs a common underlying model architecture, represents an improvement over  
87 previous studies of the impact of model resolution on the representation of topographic  
88 flow distortion that have used reanalyses with different data assimilation systems and  
89 model parameterizations [Bromwich *et al.*, 2015; Moore *et al.*, 2016; Moore *et al.*, 2015].

90 **Results**

91 Figure 3 presents the wind rose for the Hans Island AWS data. The tendency for  
92 bidirectional flow, in the NNE or SSW directions, is apparent as is the preference for  
93 northerly flow. This directionality is consistent with the orientation of the Kennedy  
94 Channel in the vicinity of Hans Island (Figure 2). The mean wind speed is  $\sim 5.8 \text{ ms}^{-1}$  with  
95 a 95<sup>th</sup> percentile wind speed of  $13.8 \text{ ms}^{-1}$ . For northerly flow, the maximum wind speed  
96 was  $29.4 \text{ ms}^{-1}$  with a 95<sup>th</sup> percentile wind speed of  $15.4 \text{ ms}^{-1}$ . The corresponding values for  
97 southerly flow were  $22.4 \text{ ms}^{-1}$  and  $10.4 \text{ ms}^{-1}$ .

98 Figure 4 provides scatterplots of the observed surface wind speed at the AWS with  
99 the 10m wind speeds from the three model datasets: the eERA5 with a horizontal resolution  
100 of  $\sim 60\text{km}$ ; the ERA5 with a horizontal resolution of  $\sim 30\text{km}$  and the ECOA with a  
101 horizontal resolution of  $\sim 9\text{km}$ . Statistics that provide quantitative measures of the  
102 goodness of the fit are shown. These include the root-mean-square (rms) and bias errors as  
103 well as the least-squares slope and the correlation coefficient  $r$ . A least-squares slope of 1  
104 implies a one-to-one relationship exists between the observations and model output.

105 The results show that both the eERA5 (Fig 4a) and the ERA5 (Fig 4b) have a  
106 marked tendency to underestimate the wind speed at the AWS site with the ERA5 having  
107 a slightly better fit. For example, the rms error for eERA5 is  $4.56 \text{ ms}^{-1}$  with a least-squares  
108 slope of 0.44; while for ERA5 the corresponding values are  $4.09 \text{ ms}^{-1}$  and 0.55. The bias

109 errors for both of these datasets was  $\sim 3 \text{ ms}^{-1}$ . By comparison, the ECOA (Fig 4c) has an  
110 improved fit to the data with a rms error was  $2.18 \text{ ms}^{-1}$  and a bias error of  $0.17 \text{ ms}^{-1}$  as well  
111 as a reduced tendency to underestimate the wind speed at the AWS site indicated by the  
112 least-squares slope of 0.8. The correlation coefficient increases from 0.67 for the eERA5  
113 to 0.79 for the ERA5 to 0.87 for the ECOA.

114 The AWS was situated on an island at a height of approximately 170m above sea-  
115 level that is not resolved in the models and hence there is a concern that the 10m winds  
116 may have a systematic low bias. The corresponding scatterplots for the 100m wind speeds  
117 from the three datasets are shown in Figure 5. As compared with the 10m winds, there is  
118 an improvement in the fit that is most pronounced for the eERA5 and ERA5 datasets, where  
119 the rms errors are reduced to  $3.53 \text{ ms}^{-1}$  and  $2.97 \text{ ms}^{-1}$  respectively, while the least squares  
120 slopes increased to 0.44 and 0.55. For the ECOA, the least squares slope increased to 1.03.  
121 However, the rms and bias errors increased to  $3.64 \text{ ms}^{-1}$  and  $2.51 \text{ ms}^{-1}$  respectively. There  
122 is no material change in the correlation coefficients for the 100m windspeed from the  
123 corresponding value for the 10m windspeed.

124 As noted above, the flow in the vicinity of Hans Island has a pronounced  
125 bidirectionality. Figure 6 shows the scatterplots of the observed meridional and zonal  
126 components at the AWS with the corresponding components of the 10m wind from the  
127 three model datasets. Similar results were found for the comparison with the components  
128 of the model 100m winds (not shown). In general, the characteristics noted above with  
129 respect to the 10m wind speed hold for the components. In particular, there is a reduction  
130 in the rms and bias errors as well as an increase in the least-squares slopes as one transitions  
131 from the lower resolution to higher resolution datasets. In addition, the fit to the zonal

132 component is generally poorer than that for the meridional component, a characteristic that  
133 is most noticeable for the eERA5 and ERA5 datasets.

134 It is of interest to characterize the spatial variability in the 10m wind field in the  
135 vicinity of Hans Island as represented in the three model datasets. To accomplish this, one-  
136 point correlation maps [Wallace and Gutzler, 1981] of the 10m wind speed at Hans Island  
137 with the wind speed at other grid points in the Nares Strait region were calculated (Figure  
138 7). Also shown is the 0.5 and 0.7 correlation coefficient contours that encompasses the  
139 area in which the variability in the 10m wind speed at Hans Island can explain ~25% and  
140 ~50% of the variability in the 10m wind speeds [De Benedetti and Moore, 2020]. The 0.7  
141 correlation coefficient contours were also fit to ellipses using a least-squares approach  
142 [Gander et al., 1994] so as to allow for a determination of their eccentricity and orientation  
143 [De Benedetti and Moore, 2017].

144 The results for all three model data sets indicate a high degree of correlation in the  
145 wind speed along Nares Strait with that at Hans Island. For eERA5, the region with  
146 correlation coefficients greater than 0.5 and 0.7 extend over both Ellesmere Island and  
147 Greenland resulting, for example, in an elliptical fit to the  $r=0.7$  contour that has an  
148 eccentricity of 0.79 (Fig 7a). This characteristic of the spatial correlation of the wind field,  
149 i.e. the correlation over the regions of high topography adjoining Nares Strait, is reduced  
150 in ERA5 resulting in an eccentricity of 0.95 for the  $r=0.7$  contour (Fig 7b). In contrast, the  
151 0.7 contour for the ECOA is, for the most part, restricted to Nares Strait resulting in an  
152 eccentricity of 0.98 (Fig 7c). For all three datasets, there is an asymmetry in the along Nares  
153 Strait extent of the region of elevated correlation with the Hans Island 10m wind speed  
154 with the region of elevated correlation extending farther to the south as compared to the

155 north. Indeed for the ECOA, the 10m wind speeds as far south as Smith Sounds are  
156 correlated with that at Hans Island, at the r=0.5 level.

157 To test the hypothesis that this asymmetry is the result of the preference for  
158 northerly flow at Hans Island, the one-point correlation maps were recalculated for times  
159 in which either northerly or southerly flow was present at Hans Island. Results are shown  
160 in Figure 8 for the ECOA dataset. The one-point correlation map for northerly flow (Fig  
161 8a) is very similar to that when there is no preference to the wind direction (Fig 7c). In  
162 contrast, the one-point correlation map for southerly flow (Fig 8b) indicates that the region  
163 of elevated correlation in the wind extends northward over the southern Lincoln Sea as  
164 well as adjacent regions of north Greenland.

165 **Discussion**

166 The Nares Strait wind field plays an important role in modulating the export of  
167 thick multi-year sea ice from the Last Ice Area situated to its north as well as in maintaining  
168 the NOW located at its southern end [Barber *et al.*, 2001; Samelson *et al.*, 2006]. There  
169 has been a significant loss of multi-year ice from the Arctic in recent years [Kwok, 2018]  
170 as well as an increase in ice export along Nares Strait [Moore *et al.*, 2021] and there is also  
171 evidence that the NOW is increasing in area [April *et al.*, 2019]. The remoteness of the  
172 Nares Strait region has limited our ability to characterize the wind field thereby leading to  
173 uncertainty in its role in the changes to the ice in the region that are now being observed in  
174 the region. The narrowness of the strait (Figure1) leads to high winds arising from  
175 interactions with the topography along its coast that remain a challenge for models to  
176 capture [Samelson *et al.*, 2006; Samelson and Barbour, 2008]. In this paper, we have used  
177 wind observations from an automatic weather station situated on Hans Island, in the middle

178 of Nares Strait (Figure 1 & 2), to document the variability in wind field along the strait and  
179 the ability of numerical models to represent this variability.

180 The Hans Island wind observations confirm that the flow along the strait is  
181 bidirectional, with preferred directions from the NNE or SSW and that northerly flow is  
182 most common (Figure 3). There is evidence that extreme events with either directionality  
183 occur with wind speeds in excess of  $20 \text{ ms}^{-1}$ . One such northerly wind event destroyed an  
184 ice camp that had been established along the Kennedy Channel in April 2005 [Melling,  
185 2011]. The Hans Island data confirm historical observations as to the occurrence of high  
186 speed wind events along Nares Strait [Bessels, 1876; Greely, 1888; Steffen, 1985].

187 To assess the role that horizontal resolution plays in the ability of models to  
188 represent the variability in the wind observed at Hans Island, three different versions of the  
189 ECMWF's IFS were considered with resolutions of  $\sim 60 \text{ km}$  (eERA5),  $\sim 30 \text{ km}$  (ERA5) and  
190  $\sim 9 \text{ km}$  (ECOA). The common lineage of the models allows one to control for biases arising  
191 from difference in model architecture and parameterizations [Bromwich *et al.*, 2015; Moore  
192 *et al.*, 2016; Moore *et al.*, 2015]. As discussed above, the observations were made at a  
193 height of 173m above sea-level on a small island that is not resolved by any of the models.  
194 For this reason, comparisons were made both for the 10m and 100m winds from the three  
195 versions of the IFS.

196 The comparison for the 10m wind (Figure 4) shows a measurable improvement in  
197 the representation of the observations with increasing model resolution with the largest  
198 jump occurring between the ERA5 (resolution  $\sim 25 \text{ km}$ ) and the ECOA (resolution  $\sim 9 \text{ km}$ ).  
199 For example, the rms error decreased from  $4.09 \text{ ms}^{-1}$  for the ERA5 to  $2.18 \text{ ms}^{-1}$  for the  
200 ECOA; while the slope of the least squares linear fit increased from 0.39 for the ERA5 to

201 0.8 for the ECOA. The latter characteristic implies that the eERA5 and the ERA5 have a  
202 tendency to underestimate the wind speed during high wind speed events. Nevertheless,  
203 all three versions of the IFS have relatively high correlation coefficients, varying from 0.67  
204 for the eERA5 to 0.87 for the ECOA, suggesting that a degree of linearity exists between  
205 model and observations.

206 The comparison with the 100m wind (Fig 5) indicates an improvement in the fit to  
207 the data for the eERA5 and ERA5 with decreases in the rms error and increases in the slope  
208 of the least squares linear fit as compared to the 10m wind. In contrast, there was an  
209 increase in the rms and bias errors for the ECOA. This implies that the 100m winds in the  
210 ECOA systematically overestimated the wind speed as compared to the observations. This  
211 suggests that the ECOA is unable to represent the fine-scale characteristics of the flow  
212 distortion due to Hans Island [Beljaars *et al.*, 1987] resulting in a systematic overestimation  
213 of the 100m wind speed as compared to the observations. The underestimation of the  
214 100m wind speeds at by the lower-resolution eER5 and ERA5 datasets is such as to mask  
215 this effect.

216 The comparison with the components of the wind (Fig 6) shows the same  
217 improvement with increasing resolution with the fit to the meridional component being  
218 systematically better than the zonal component for the eERA5 and ERA5. This suggests  
219 that these lower resolution datasets are unable to represent the channeling of the wind by  
220 the topography along the strait.

221 The one-point correlation maps of the 10m wind field (Fig 7) confirm this  
222 characteristic in that both the eERA5 and ERA5 have regions of high correlation that spill  
223 out over the topography along the strait. In contrast for the ECOA, the region of high

224 correlation is restricted, for the most part, to Nares Strait. The eccentricities for the  
225 elliptical fits to the  $r=0.7$  contour, that range from 0.79 for the eERA5 to 0.98 for the ECOA  
226 provide a quantitative confirmation of this characteristic. The one-point correlation maps  
227 for the ECOA 10m wind (Fig 7c and Fig 8) confirm that the Hans Island observations are  
228 representative of variability in the wind field along Nares Strait and, for southerly flow,  
229 over the southern Lincoln Sea as well.

230 The results of this study suggest that a model resolution of at least 9km is required  
231 to represent the wind field along Nares Strait providing a confirmation of the work of  
232 Samelson and Barbour [2008] who used a 6km limited area numerical weather prediction  
233 model to develop a 2-year climatology of the regional wind field as well as the study of  
234 Moore and Våge [2018] that used the 9km ECOA data to represent air-sea interaction over  
235 the NOW. It also suggests that climatologies [Barber *et al.*, 2001; Preußen *et al.*, 2015]  
236 and ice/ocean models [Crowley *et al.*, 2016; Dumont *et al.*, 2010; Grivault *et al.*, 2018] of  
237 Nares Strait that are based on or forced by atmospheric datasets with horizontal resolutions  
238 coarser than 9km may underestimate wind-driven process active in the region.

239 **Methods**

240 The Hans Island AWS was installed by a joint American, Canadian, Danish and  
241 U.K. team in May 2008 [Wilkinson *et al.*, 2009]. The surface air temperature, wind speed  
242 and direction as well as solar radiation and surface pressure are available starting in  
243 September 2014 at a 30 min interval. There are numerous data gaps as well as a period of  
244 approximately 3 months, May-July, during 2016 when the sign of the zonal wind  
245 component was intermittently reversed. For this study, we will use the wind speed and  
246 direction data for the period September 2 2014-September 30 2020 with the exception of

247 the 3 month period with bad wind direction data during 2016. The data was subsampled  
248 to a 6-hourly interval.

249 In this paper, we will make use of 3 model datasets based on the ECMWF's  
250 Integrated Forecast System (IFS). Included is the new fifth generation reanalysis from the  
251 ECMWF or ERA5 with a horizontal resolution of ~30km, as well as its ensemble version,  
252 eERA5 with a horizontal resolution of ~60km, [*Hersbach et al.*, 2020], and the current  
253 version of their operational analysis or ECOA, with a horizontal resolution of ~9km, [*Holm*  
254 *et al.*, 2016]. The eERA5 ensemble consists of an unperturbed member and 9 perturbed  
255 members. For this work, we made use of the unperturbed member. For this study, we used  
256 the model data for the period 2016-2020. The eERA5 and ERA5 datasets are based on  
257 Cycle 41r2 of the IFS. Being an operational product, the ECOA data is based on a number  
258 of different cycles of the IFS from Cycle 41r2 up to Cycle47r1. No material changes to  
259 the IFS, that would impact the present study, ccurred over the period 2016-2020.

260 For this study, the 6-hourly 10 m winds and 100m from these three datasets were  
261 interpolated to the location of Hans Island and the data was used at those times for which  
262 there are observations. In total, ~ 550 days worth of data was included in this study. The  
263 AWS was situated at a height of approximately 170m above sea level [*Wilkinson et al.*,  
264 2009]. The models do not resolve Hans Island and so will not represent the flow distortion  
265 associated with the island. However, the use of both the 10m and 100m model winds will  
266 provide insight on the impact that this flow distortion has on the wind field in the region.

267 **References**  
268

269 April, A., B. Montpetit, and D. Langlois (2019), Linking the Open Water Area of the  
270 North Open Water Polynya to Climatic Parameters using a Multiple Linear Regression

- 271 Prediction Model, *Atmosphere-Ocean*, 57(2), 91-100,  
272 doi:10.1080/07055900.2019.1598332.
- 273 Barber, D. G., J. M. Hanesiak, W. Chan, and J. Piwowar (2001), Sea - ice and  
274 meteorological conditions in Northern Baffin Bay and the North Water polynya between  
275 1979 and 1996, *Atmosphere-Ocean*, 39(3), 343-359,  
276 doi:10.1080/07055900.2001.9649685.
- 277 Beljaars, A., J. Walmsley, and P. Taylor (1987), A mixed spectral finite-difference model  
278 for neutrally stratified boundary-layer flow over roughness changes and topography,  
279 *Boundary-Layer Meteorology*, 38(3), 273-303.
- 280 Bessels, E. (1876), Scientific Results of the United States Arctic Expedition, Steamer  
281 Polaris, *CF Hall Commanding. Vol. 1: Physical Observations*.
- 282 Bromwich, D. H., A. Wilson, L.-S. Bai, G. W. K. Moore, and P. Bauer (2015), A  
283 comparison of the regional Arctic System Reanalysis and the global ERA-Interim  
284 Reanalysis for the Arctic, *Quarterly Journal of the Royal Meteorological Society*,  
285 142(695), 644-658.
- 286 Crowley, P., G. Rowe, and G. Geospatial (2016), Modeling Oil Spill Trajectories in  
287 Baffin Bay and Lancaster Sound.
- 288 De Benedetti, M., and G. Moore (2017), Impact of resolution on the representation of  
289 precipitation variability associated with the ITCZ, *Geophysical Research Letters*, 44(24),  
290 12,519-512,526.
- 291 De Benedetti, M., and G. Moore (2020), Impact of model resolution on the representation  
292 of the wind speed field: An example from the United Kingdom, *Quarterly Journal of the*  
293 *Royal Meteorological Society*, 146(726), 367-379.

- 294 Dumont, D., Y. Gratton, and T. E. Arbetter (2010), Modeling Wind-Driven Circulation  
295 and Landfast Ice-Edge Processes during Polynya Events in Northern Baffin Bay, *Journal*  
296 *of Physical Oceanography*, 40(6), 1356-1372, doi:10.1175/2010JPO4292.1.
- 297 Gander, W., G. H. Golub, and R. Strebel (1994), Least-squares fitting of circles and  
298 ellipses, *BIT Numerical Mathematics*, 34(4), 558-578, doi:10.1007/BF01934268.
- 299 Greely, A. (1888), *Proceedings of the United States Expedition to Lady Franklin Bay,*  
300 *Grinnell Land*, Government Printing Office, Washington.
- 301 Grivault, N., X. Hu, and P. G. Myers (2018), Impact of the surface stress on the volume  
302 and freshwater transport through the Canadian Arctic Archipelago from a high -  
303 resolution numerical simulation, *Journal of Geophysical Research: Oceans*, 123(12),  
304 9038-9060.
- 305 Hersbach, H., B. Bell, P. Berrisford, S. Hirahara, A. Horányi, J. Muñoz - Sabater, J.  
306 Nicolas, C. Peubey, R. Radu, and D. Schepers (2020), The ERA5 global reanalysis,  
307 *Quarterly Journal of the Royal Meteorological Society*, 146(730), 1999-2049.
- 308 Holm, E. V., R. Forbes, S. Lang, L. Magnusson, and S. Malardel (2016), New model  
309 cycle brings higher resolution *ECMWF Newsletter*, 147.
- 310 Ingram, R. G., J. Bâcle, D. G. Barber, Y. Gratton, and H. Melling (2002), An overview of  
311 physical processes in the North Water, *Deep Sea Research Part II: Topical Studies in*  
312 *Oceanography*, 49(22), 4893-4906, doi:[http://dx.doi.org/10.1016/S0967-0645\(02\)00169-8](http://dx.doi.org/10.1016/S0967-0645(02)00169-8).
- 314 Ito, H. (1982), Wind Through a Channel—Surface Wind Measurements in Smith Sound  
315 and Jones Sound in Northern Baffin Bay, *Journal of Applied Meteorology*, 21(8), 1053-  
316 1062, doi:10.1175/1520-0450(1982)021<1053:WTACWM>2.0.CO;2.

- 317 Kwok, R. (2018), Arctic sea ice thickness, volume, and multiyear ice coverage: losses  
318 and coupled variability (1958–2018), *Environmental Research Letters*, 13(10), 105005.
- 319 Kwok, R., L. Toudal Pedersen, P. Gudmandsen, and S. S. Pang (2010), Large sea ice  
320 outflow into the Nares Strait in 2007, *Geophysical Research Letters*, 37(3), n/a-n/a,  
321 doi:10.1029/2009GL041872.
- 322 Lindsay, R., and A. Schweiger (2015), Arctic sea ice thickness loss determined using  
323 subsurface, aircraft, and satellite observations, *The Cryosphere*, 9(1), 269-283.
- 324 Maslanik, J., J. Stroeve, C. Fowler, and W. Emery (2011), Distribution and trends in  
325 Arctic sea ice age through spring 2011, *Geophysical Research Letters*, 38(13),  
326 doi:10.1029/2011GL047735.
- 327 Melling, H. (2011), The Best Laid Schemes: A Nares Strait Adventure, *Oceanography*.
- 328 Moore, G., D. H. Bromwich, A. B. Wilson, I. Renfrew, and L. Bai (2016), Arctic System  
329 Reanalysis improvements in topographically forced winds near Greenland, *Quarterly  
330 Journal of the Royal Meteorological Society*, 142(698), 2033-2045.
- 331 Moore, G., S. E. L. Howell, M. Brady, X. Xu, and K. McNeil (2021), Anomalous  
332 collapses of Nares Strait ice arches leads to enhanced export of Arctic sea ice, *Nature  
333 Communications*, 12(1), 1-8.
- 334 Moore, G., and K. McNeil (2018), The early collapse of the 2017 Lincoln Sea ice arch in  
335 response to anomalous sea ice and wind forcing, *Geophysical Research Letters*, 45(16),  
336 8343-8351.
- 337 Moore, G., I. Renfrew, B. Harden, and S. Mernild (2015), The impact of resolution on the  
338 representation of southeast Greenland barrier winds and katabatic flows, *Geophysical  
339 Research Letters*, 42(8), 3011-3018.

- 340 Moore, G., A. Schweiger, J. Zhang, and M. Steele (2019), Spatiotemporal variability of  
341 sea ice in the arctic's last ice area, *Geophysical Research Letters*, 46(20), 11237-11243.
- 342 Moore, G. W. K., and K. Våge (2018), Impact of model resolution on the representation  
343 of the air–sea interaction associated with the North Water Polynya, *Quarterly Journal of*  
344 *the Royal Meteorological Society*, 144(714), 1474-1489,  
345 doi:<https://doi.org/10.1002/qj.3295>.
- 346 Preußer, A., G. Heinemann, S. Willmes, and S. Paul (2015), Multi-decadal variability of  
347 polynya characteristics and ice production in the north water polynya by means of  
348 passive microwave and thermal infrared satellite imagery, *Remote Sensing*, 7(12), 15844-  
349 15867.
- 350 Samelson, R. M., T. Agnew, H. Melling, and A. Münchow (2006), Evidence for  
351 atmospheric control of sea-ice motion through Nares Strait, *Geophysical Research  
Letters*, 33(2), n/a-n/a, doi:10.1029/2005GL025016.
- 353 Samelson, R. M., and P. L. Barbour (2008), Low-Level Jets, Orographic Effects, and  
354 Extreme Events in Nares Strait: A Model-Based Mesoscale Climatology, *Monthly  
Weather Review*, 136(12), 4746-4759, doi:10.1175/2007MWR2326.1.
- 356 Steffen, K. (1985), Warm water cells in the North Water, Northern Baffin Bay during  
357 winter, *Journal of Geophysical Research: Oceans*, 90(C5), 9129-9136,  
358 doi:10.1029/JC090iC05p09129.
- 359 Wallace, J. M., and D. S. Gutzler (1981), Teleconnections in the geopotential height field  
360 during the Northern Hemisphere winter, *Monthly weather review*, 109(4), 784-812.

361 Wilkinson, J., P. Gudmandsen, S. Hanson, R. Saldo, and R. Samelson (2009), Hans  
362 Island: Meteorological data from an international borderline, *Eos, Transactions American*  
363 *Geophysical Union*, 90(22), 190-191.

364 **Acknowledgements**

365 Funding was provided by the Natural Sciences and Engineering Research Council of  
366 Canada.

367 **Data Availability**

368 The author would like to thank the Scottish Association for Marine Sciences for  
369 access to the Hans Island automatic weather station data, Copernicus Data Services  
370 for access to the eERA5 and ERA5 data and the National Center for Atmospheric  
371 Research for access to the ECOA data.

372 **Competing Interests**

373 The author declares that there are no competing interests.

374 **Figure Legends**

375 Figure 1) Topography (km) of the Nares Strait region as represented in the  
376 GEBCO dataset. The location of Hans Island is indicated by the '+'. The  
377 locations of the North Water Polynya (NOW), Smith Sound (SS), the Kane  
378 Basin (KB), the Kennedy Channel (KC), the Hall Basin (HB) and the  
379 Robeson Channel (RC) are also indicated.

380 Figure 2) True-color high spatial resolution (~10m) Sentinel-2 imagery of the  
381 Kennedy Channel in the vicinity of Hans Island on August 7 19:39 GMT  
382 2020.

383      Figure 3) Windrose from the Hans Island AWS Sept 2 2014 to Sept 30 2020  
384           excluding May-July 2016.

385      Figure 4) Scatterplots of the observed 6-hourly surface wind speed and the 10m  
386           model wind speed at Hans Island. Results are shown for: a) the  
387           unperturbed member of the ensemble ERA5 reanalysis; b) the ERA5  
388           reanalysis and c) the ECOA. Data from January 1 2016-September 30  
389           2020 excluding May-July 2016 was used.

390      Figure 5) Scatterplots of the observed 6-hourly surface wind speed and the 100m  
391           model wind speed at Hans Island. Results are shown for: a) the  
392           unperturbed member of the ensemble ERA5 reanalysis; b) the ERA5  
393           reanalysis and c) the ECOA. Data from January 1 2016-September 30 2020  
394           excluding May-July 2016 was used.

395      Figure 6) Scatterplots of the observed 6-hourly components of the surface wind  
396           and the components of the 10m model wind at Hans Island. Results are  
397           shown for the meridional component for : a) the unperturbed member of the  
398           ensemble ERA5 reanalysis; b) the ERA5 reanalysis and c) the ECOA.  
399           Results are also shown for the zonal component for: d) the unperturbed  
400           member of the ensemble ERA5 reanalysis; e) the ERA5 reanalysis and f)  
401           the ECOA. Data from January 1 2016-September 30 2020 excluding May-  
402           July 2016 was used.

403      Figure 7) One-point correlation maps showing the correlation between the 10m  
404           wind speed at Hans Island and at other gridpoints in the Nares Strait region

405 as represented in the : a) eERA5; b)ERA5 and c) ECOA for the period  
406 2016-2020. The location of Hans Island is indicated by the ‘+’. The 0.5 and  
407 0.7 correlation coefficient contours are shown in white.  
408 Figure 8) One-point correlation maps showing the correlation between the 10m  
409 wind speed at Hans Island and at other gridpoints in the Nares Strait region  
410 as represented in the ECOA. Results are show for times during the period  
411 2016-2020 during which there was: a) northerly and b) southerly flow at  
412 Hans Island. The location of Hans Island is indicated by the ‘+’. The 0.5  
413 and 0.7 correlation coefficient contours are shown in white.  
414  
415

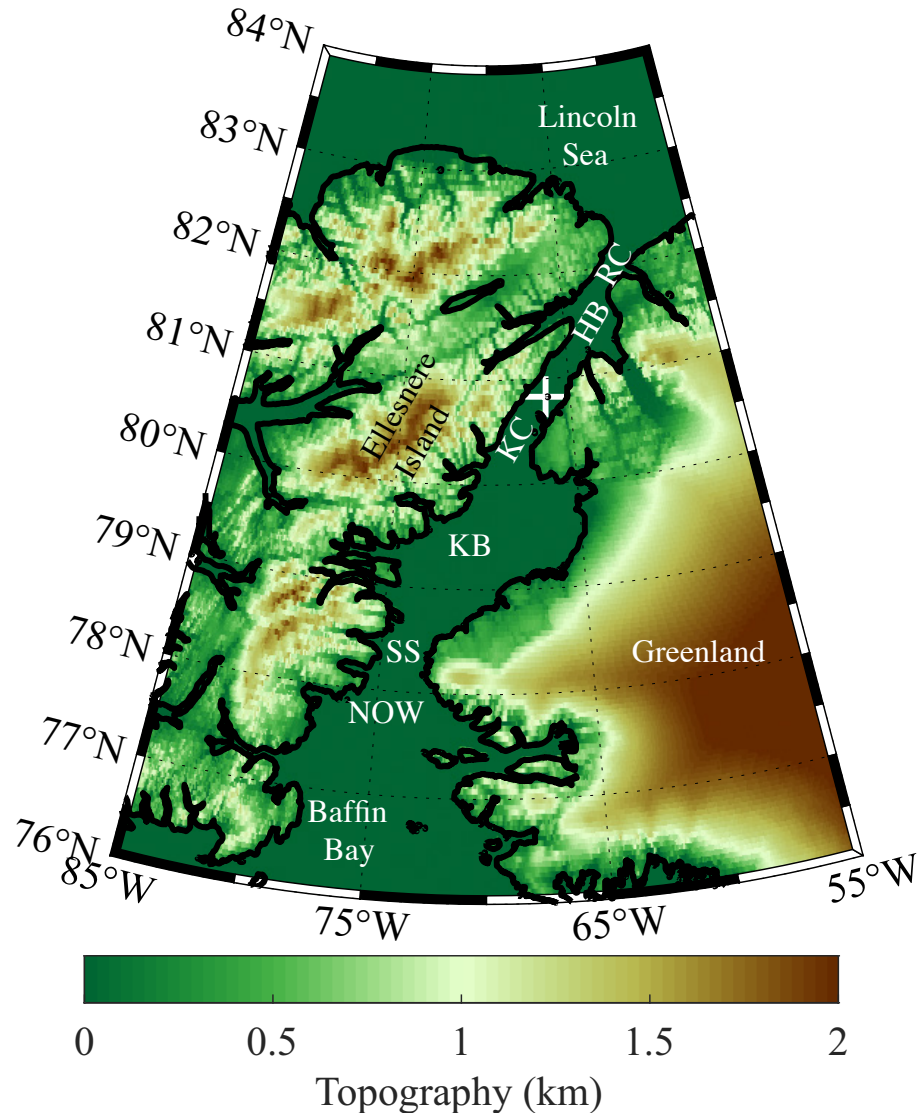


Figure 1) Topography (km) of the Nares Strait region as represented in the GEBCO dataset. The location of Hans Island is indicated by the ‘+’. The locations of the North Water Polynya (NOW), Smith Sound (SS), the Kane Basin (KB), the Kennedy Channel (KC), the Hall Basin (HB) and the Robeson Channel (RC) are also indicated.

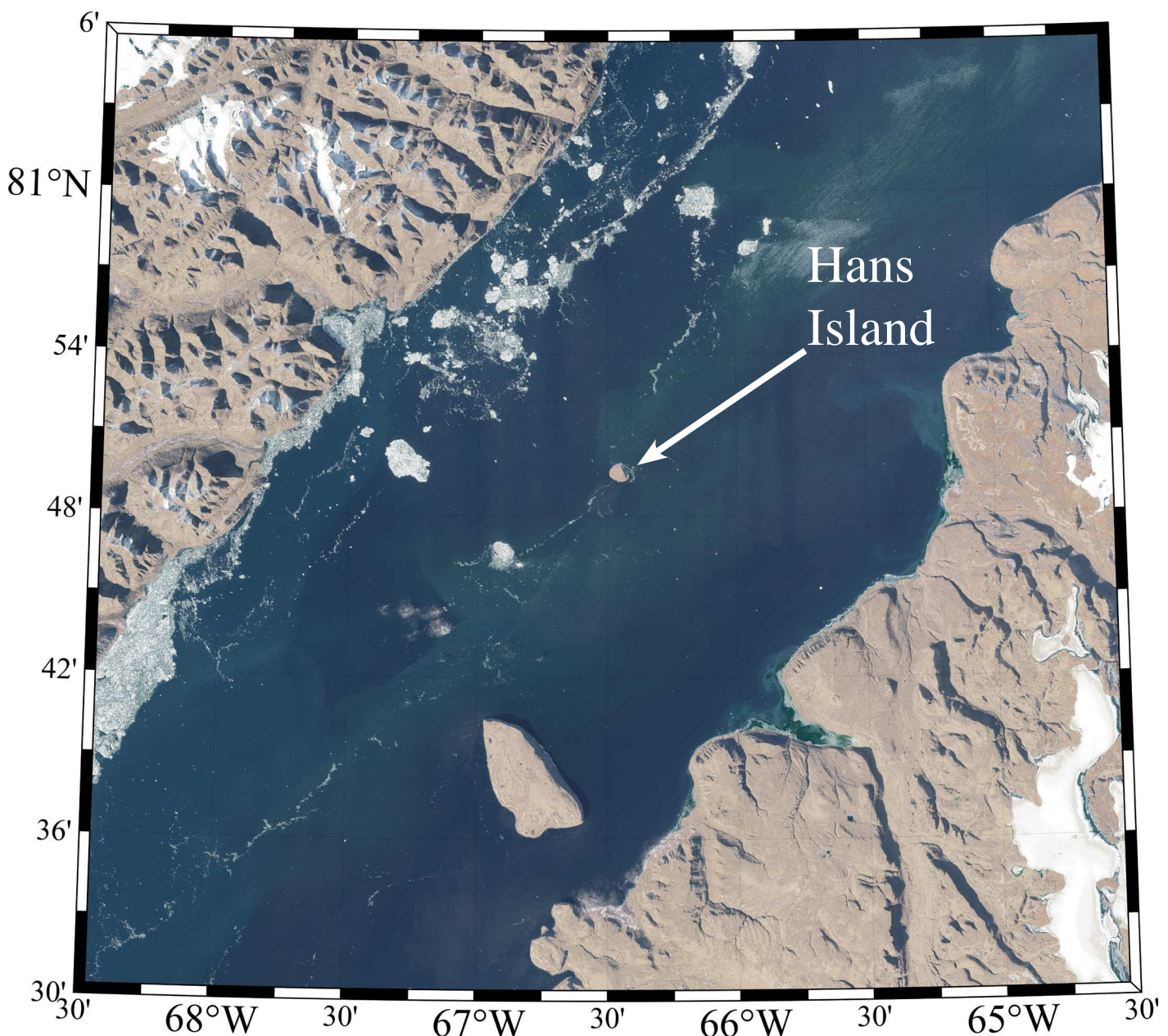


Figure 2) True-color high spatial resolution (~10m) Sentinel-2 imagery of the Kennedy Channel in the vicinity of Hans Island on August 7 19:39 GMT 2020.

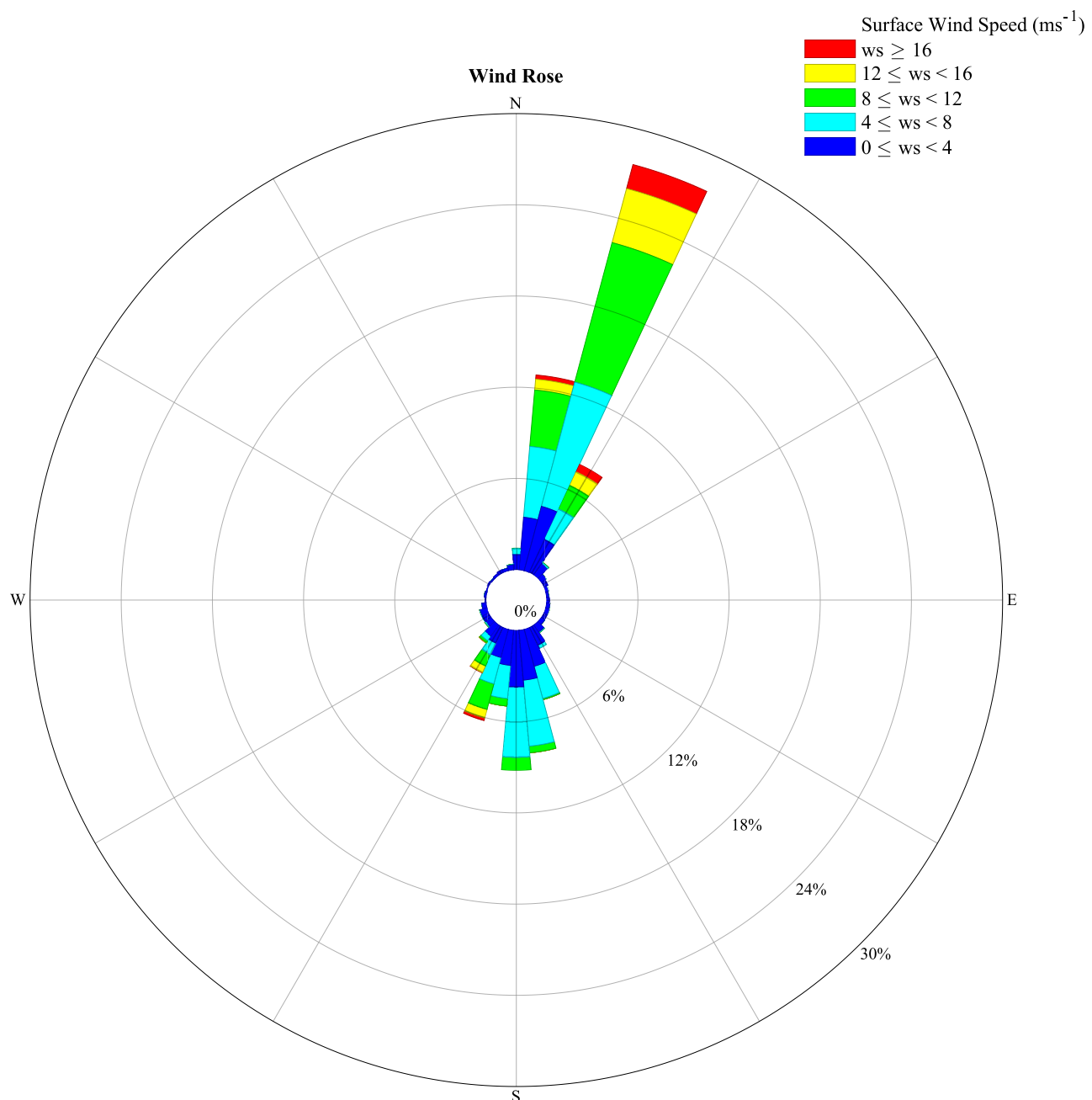


Figure 3) Windrose from the Hans Island AWS Sept 2 2014 to Sept 30 2020 excluding May-July 2016.

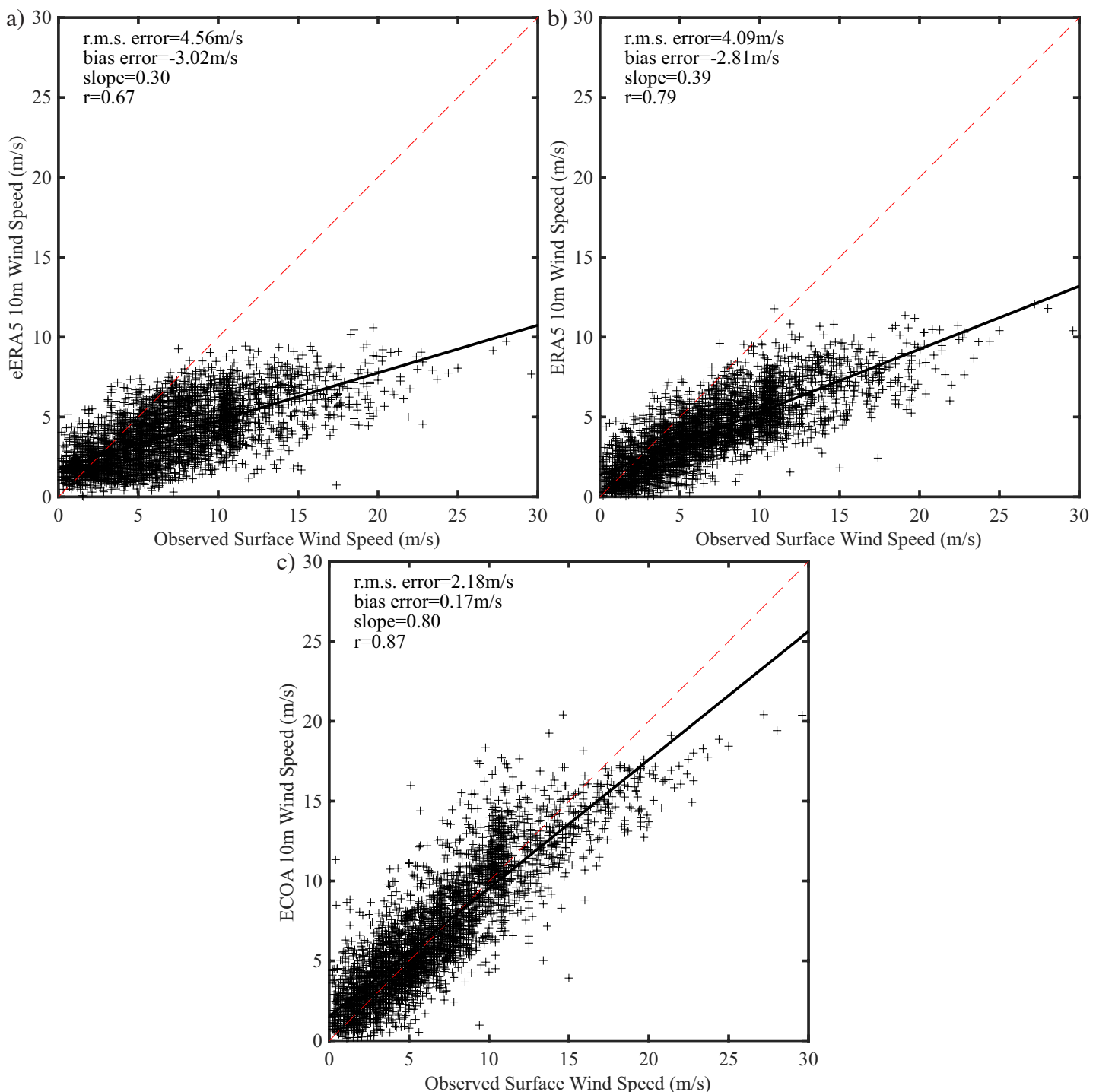


Figure 4) Scatterplots of the observed 6-hourly surface wind speed and the 10m model wind speed at Hans Island. Results are shown for: a) the unperturbed member of the ensemble ERA5 reanalysis; b) the ERA5 reanalysis and c) the ECOA. Data from January 1 2016-September 30 2020 excluding May-July 2016 was used.

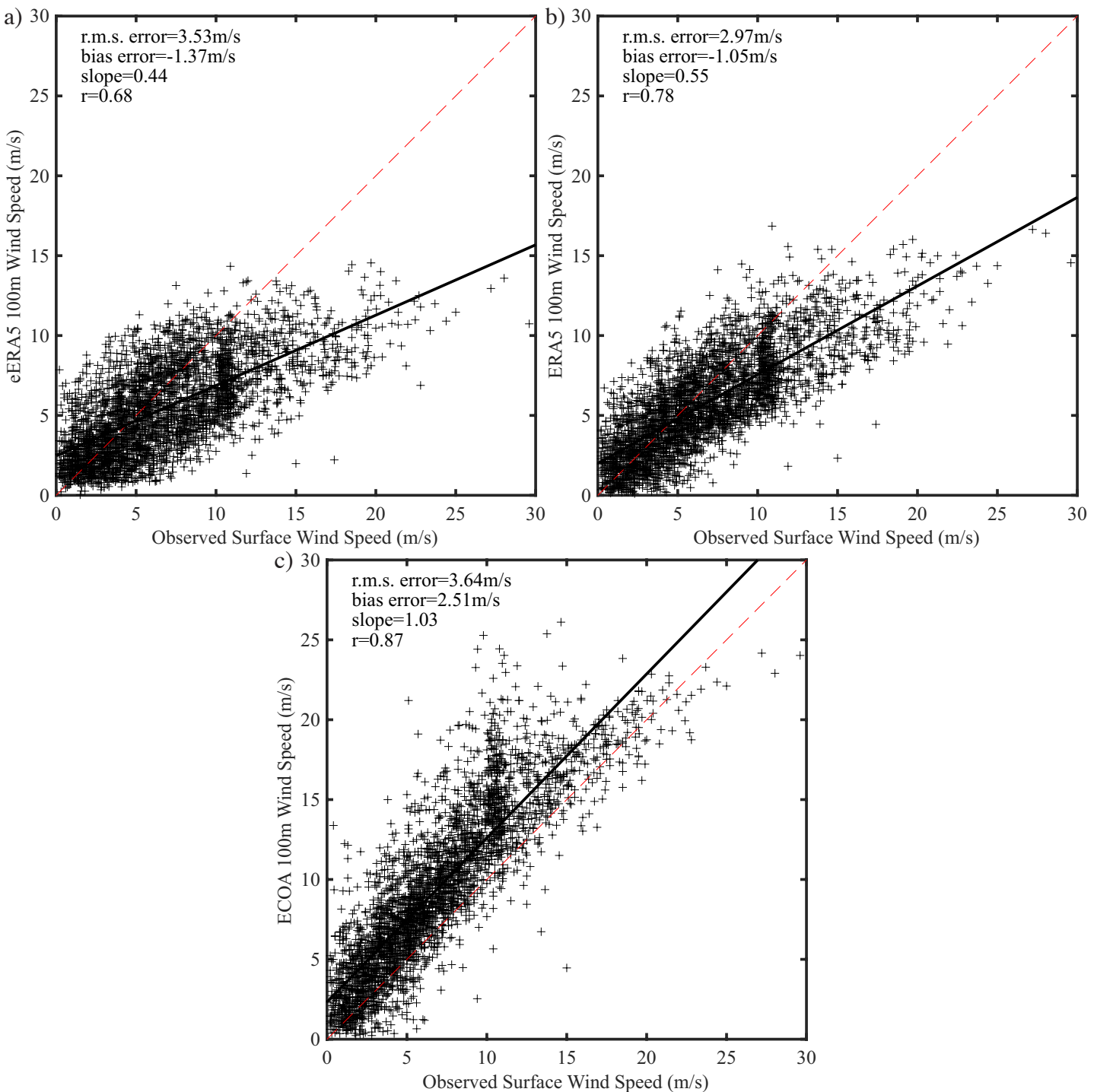
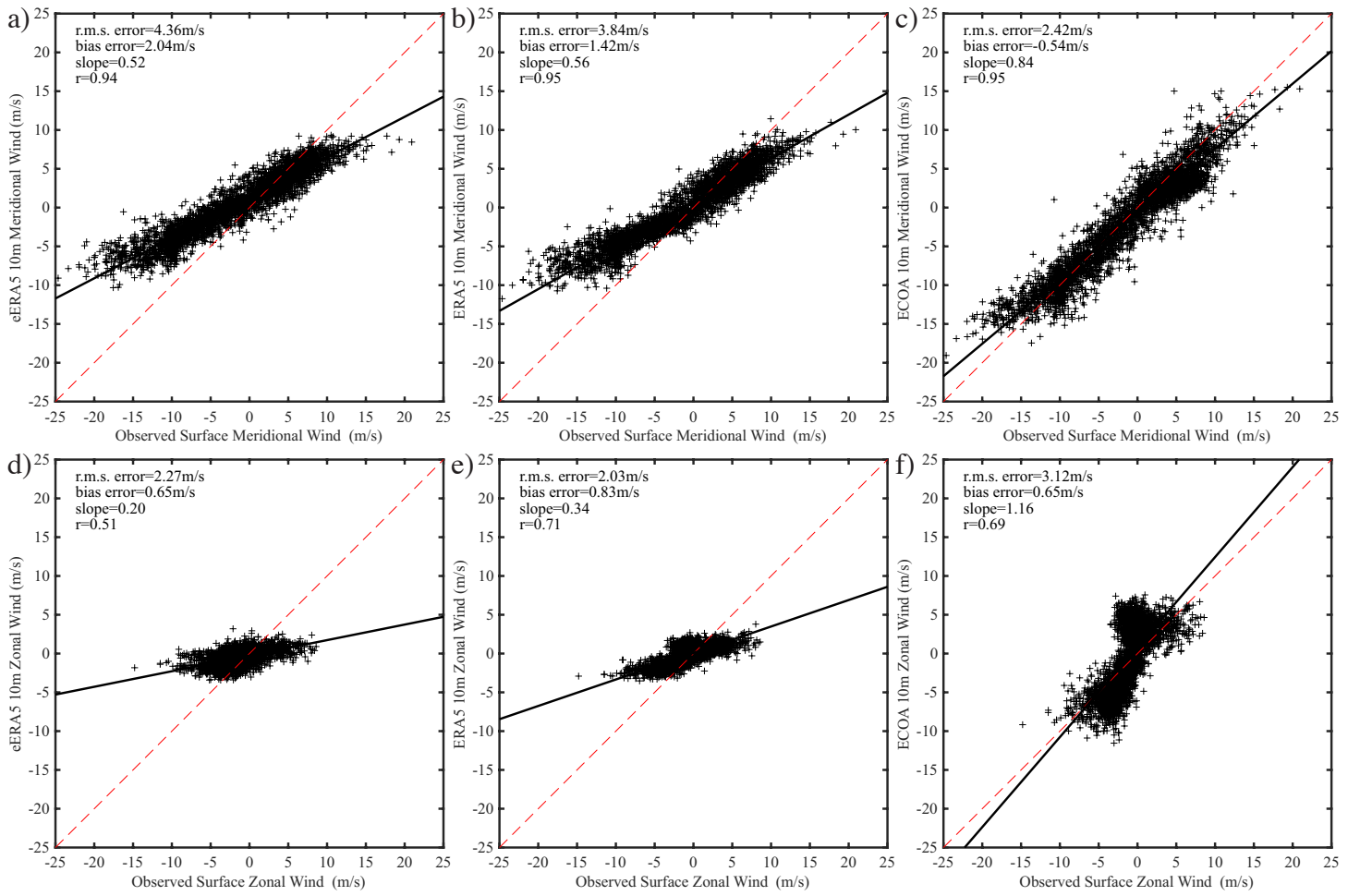


Figure 5) Scatterplots of the observed 6-hourly surface wind speed and the 100m model wind speed at Hans Island. Results are shown for: a) the unperturbed member of the ensemble ERA5 reanalysis; b) the ERA5 reanalysis and c) the ECOA. Data from January 1 2016–September 30 2020 excluding May–July 2016 was used.



**Figure 6)** Scatterplots of the observed 6-hourly components of the surface wind and the components of the 10m model wind at Hans Island. Results are shown for the meridional component for : a) the unperturbed member of the ensemble ERA5 reanalysis; b) the ERA5 reanalysis and c) the ECOA. Results are also shown for the zonal component for: d) the unperturbed member of the ensemble ERA5 reanalysis; e) the ERA5 reanalysis and f) the ECOA. Data from January 1 2016-September 30 2020 excluding May-July 2016 was used.

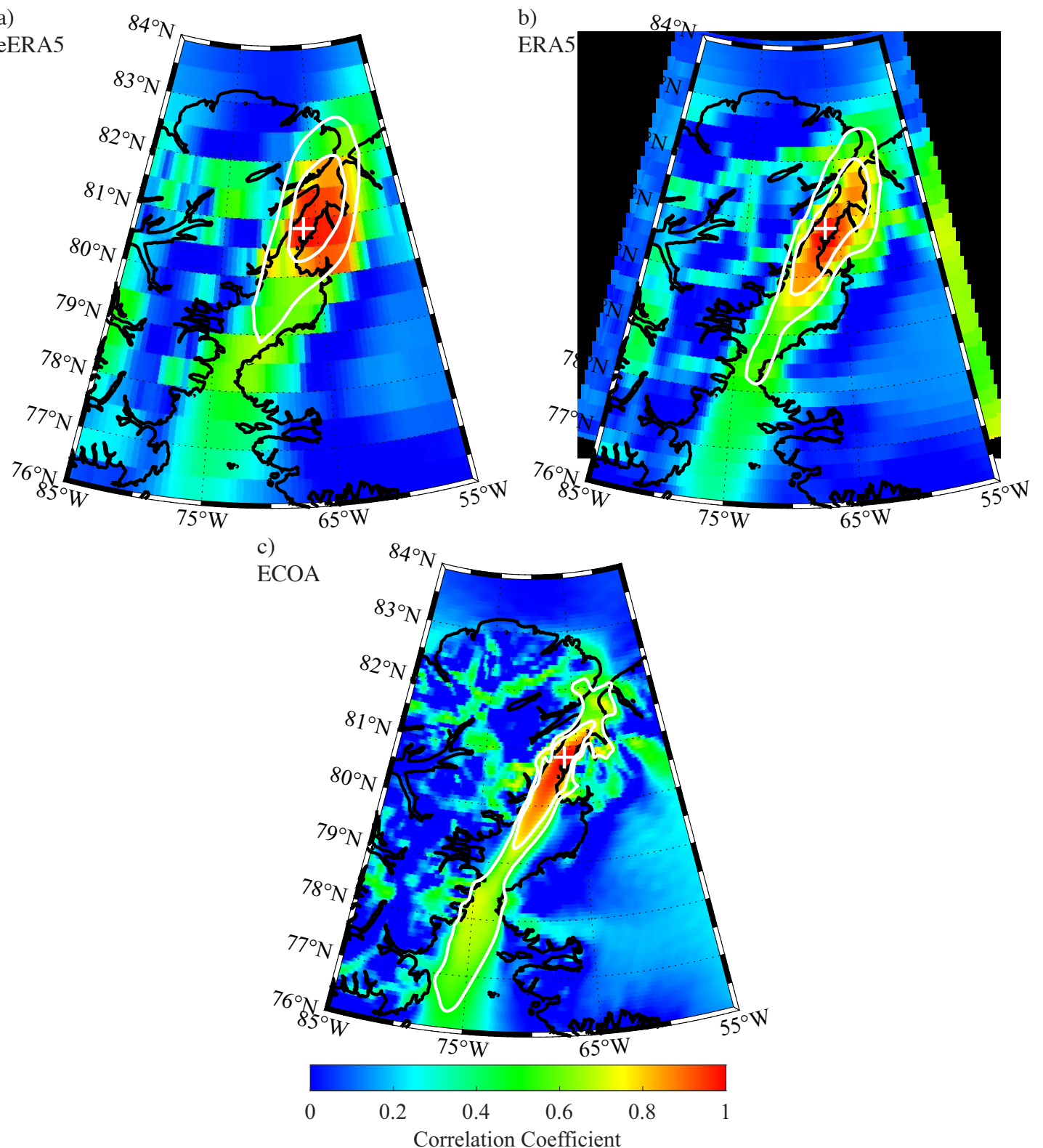


Figure 7) One-point correlation maps showing the correlation between the 10m wind speed at Hans Island and at other gridpoints in the Nares Strait region as represented in the : a) eERA5; b)ERA5 and c) ECOA for the period 2016-2020. The location of Hans Island is indicated by the '+'. The 0.5 and 0.7 correlation coefficient contours are shown in white.

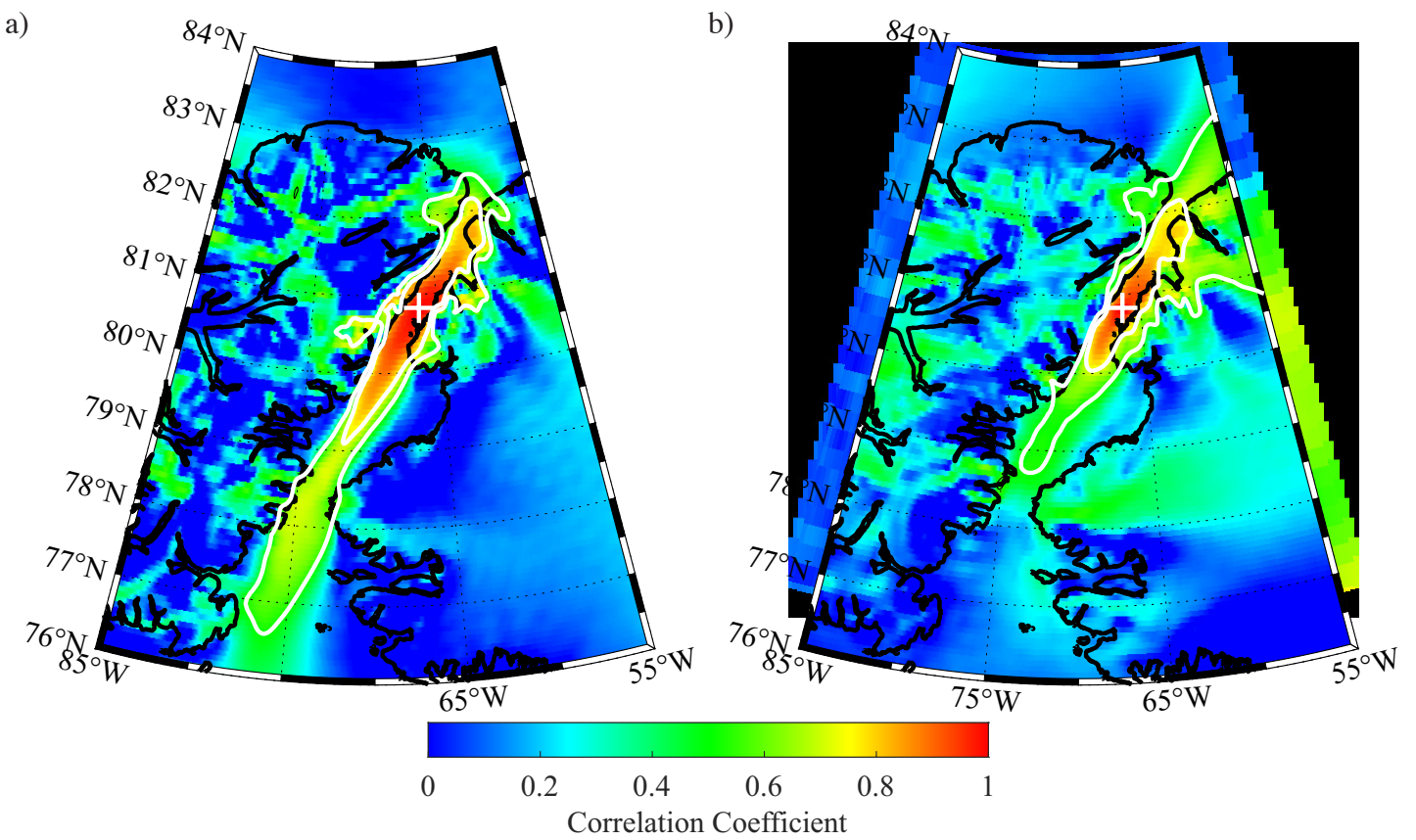


Figure 8) One-point correlation maps showing the correlation between the 10m wind speed at Hans Island and at other gridpoints in the Nares Strait region as represented in the ECCA. Results are show for times during the period 2016-2020 during which there was: a) northerly and b) southerly flow at Hans Island. The location of Hans Island is indicated by the '+'. The 0.5 and 0.7 correlation coefficient contours are shown in white.

## Figures

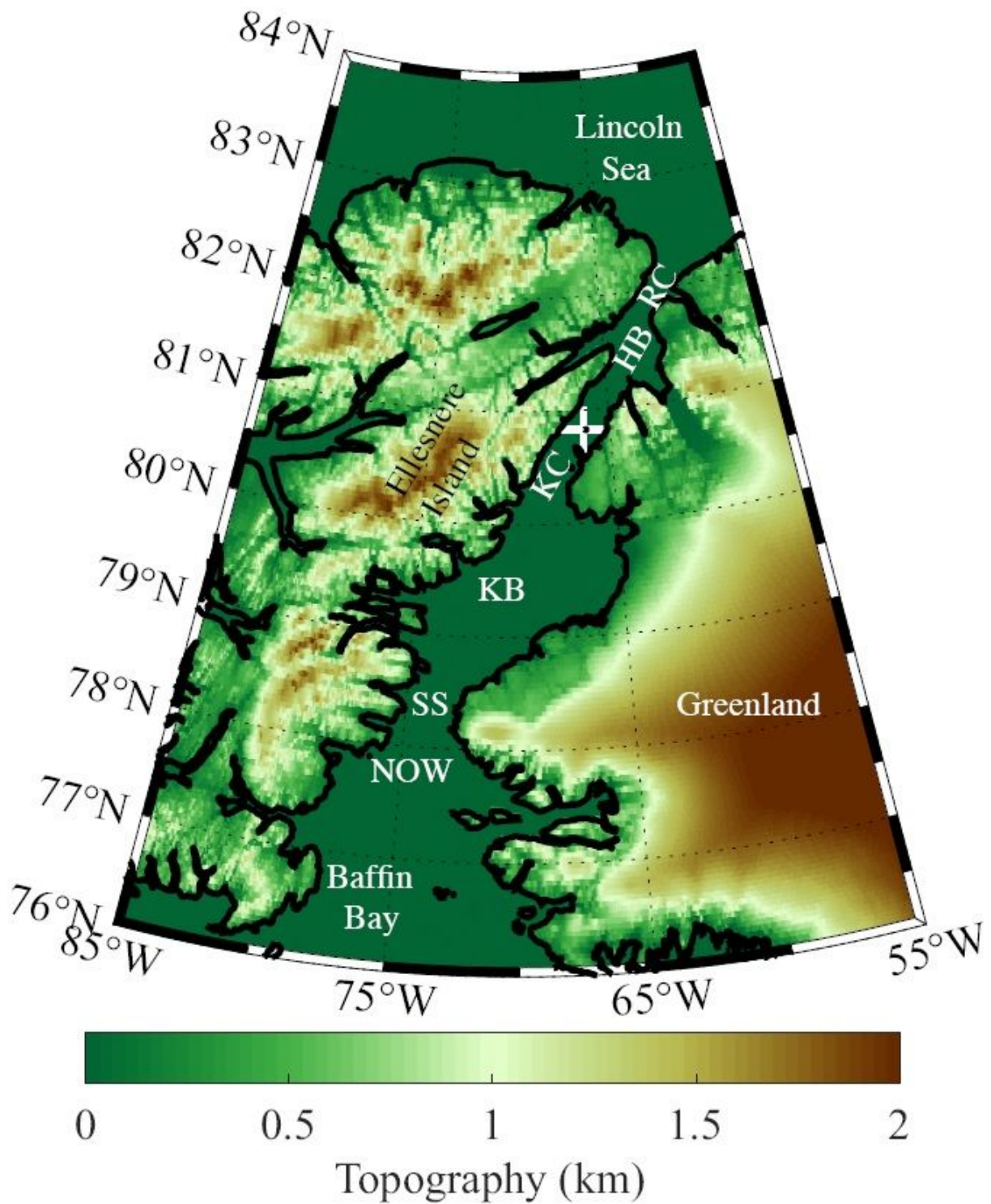
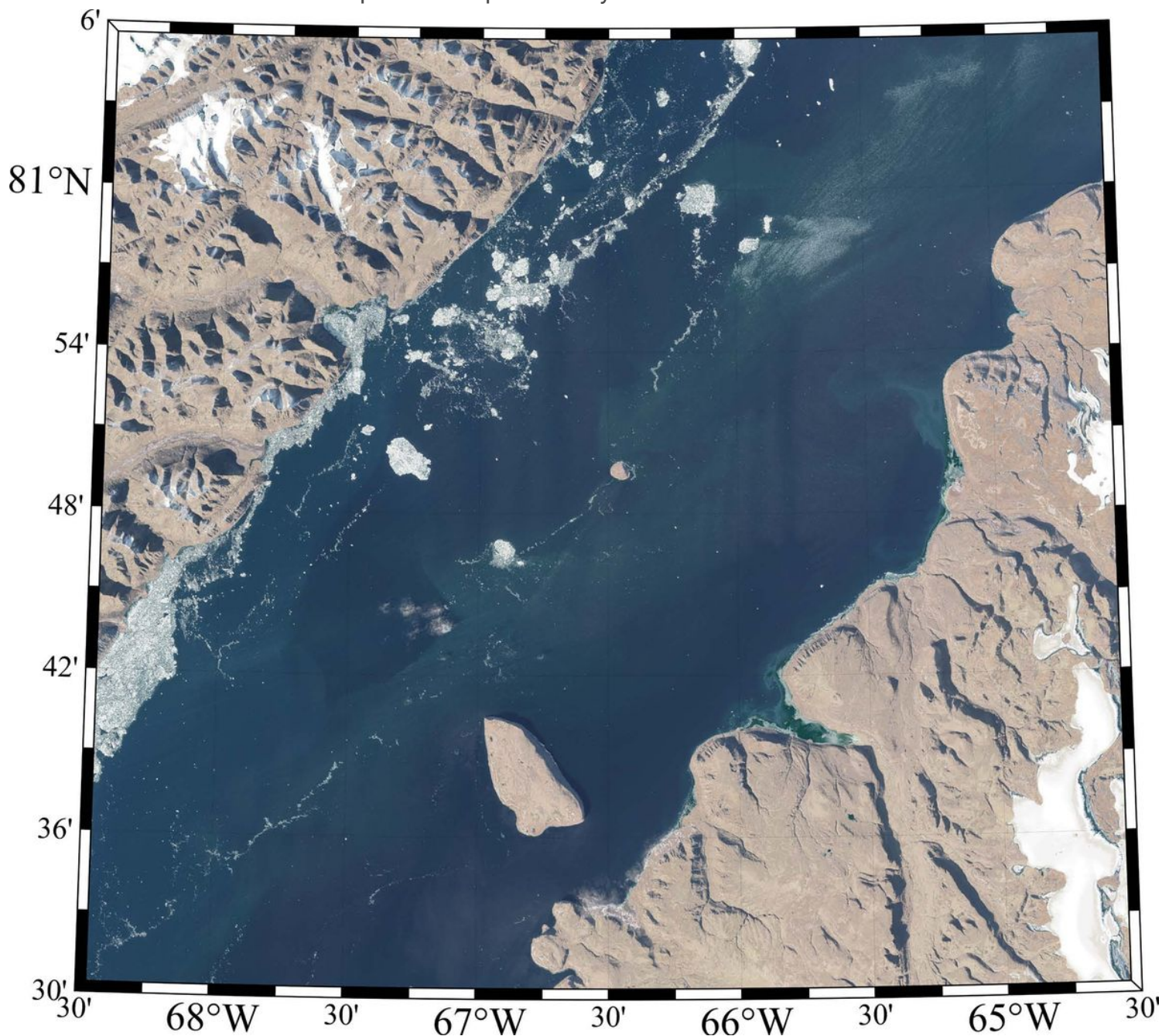


Figure 1

Topography (km) of the Nares Strait region as represented in the GEBCO dataset. The location of Hans Island is indicated by the '+'. The locations of the North Water Polynya (NOW), Smith Sound (SS), the Kane Basin (KB), the Kennedy Channel (KC), the Hall Basin (HB) and the Robeson Channel (RC) are also

indicated. Note: The designations employed and the presentation of the material on this map do not imply the expression of any opinion whatsoever on the part of Research Square concerning the legal status of any country, territory, city or area or of its authorities, or concerning the delimitation of its frontiers or boundaries. This map has been provided by the authors.



**Figure 2**

True-color high spatial resolution (~10m) Sentinel-2 imagery of the Kennedy Channel in the vicinity of Hans Island on August 7 19:39 GMT 2020. Note: The designations employed and the presentation of the material on this map do not imply the expression of any opinion whatsoever on the part of Research Square concerning the legal status of any country, territory, city or area or of its authorities, or concerning the delimitation of its frontiers or boundaries. This map has been provided by the authors.

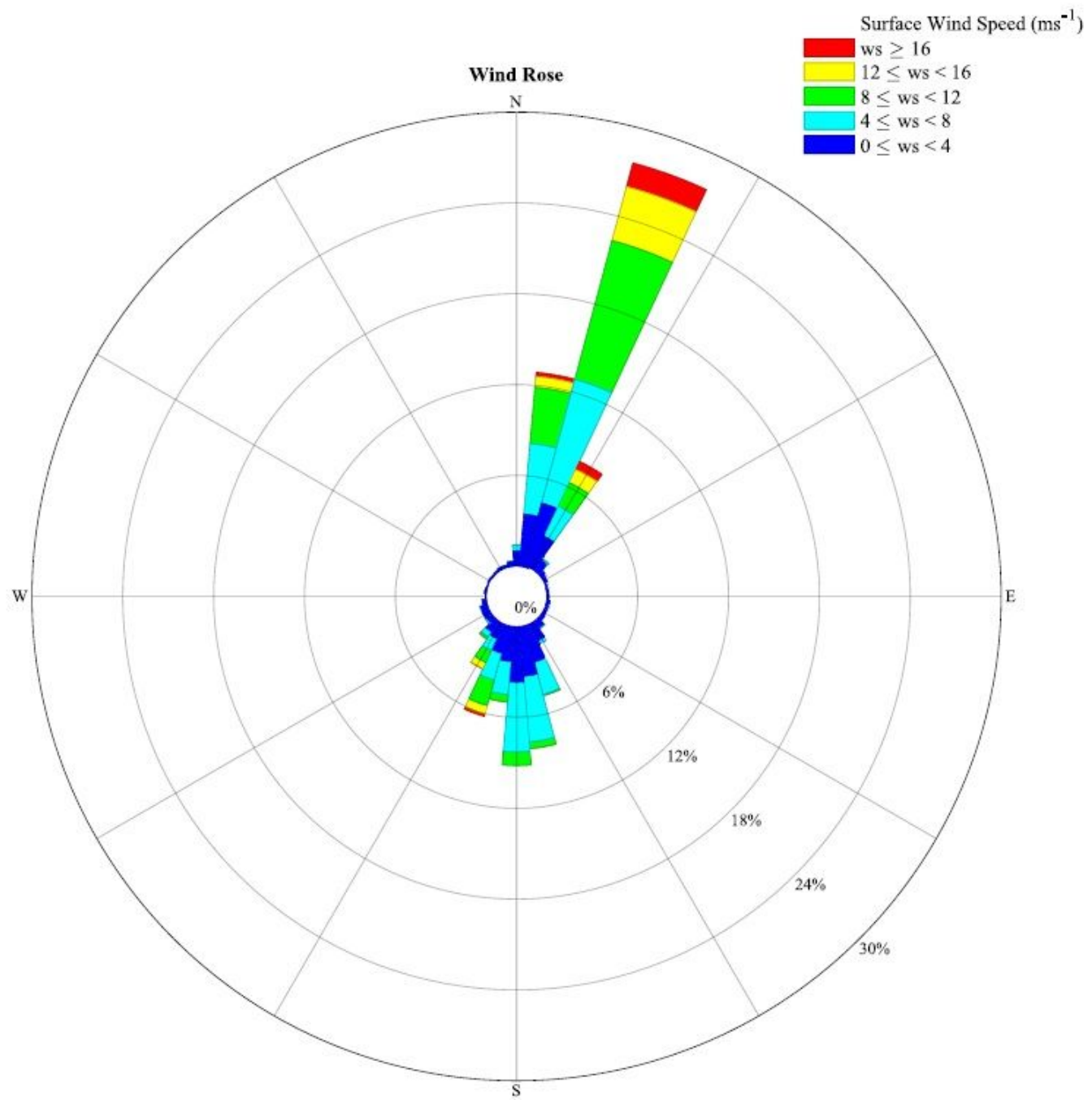


**Figure 3**

Windrose from the Hans Island AWS Sept 2 2014 to Sept 30 2020 excluding May-July 2016.

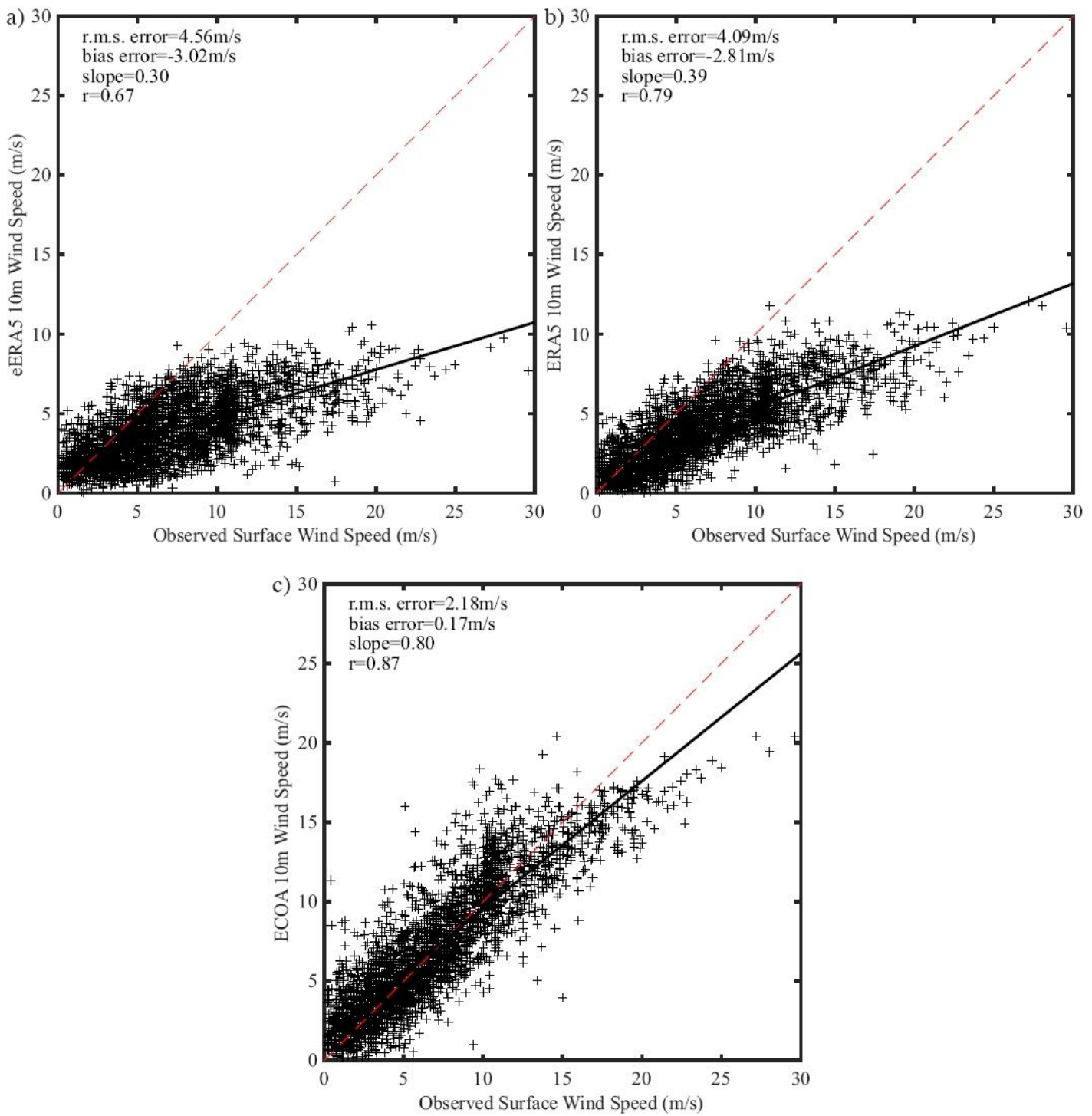


**Figure 4**

Scatterplots of the observed 6-hourly surface wind speed and the 10m model wind speed at Hans Island. Results are shown for: a) the unperturbed member of the ensemble ERA5 reanalysis; b) the ERA5 reanalysis and c) the ECOA. Data from January 1 2016-September 30 2020 excluding May-July 2016 was used.

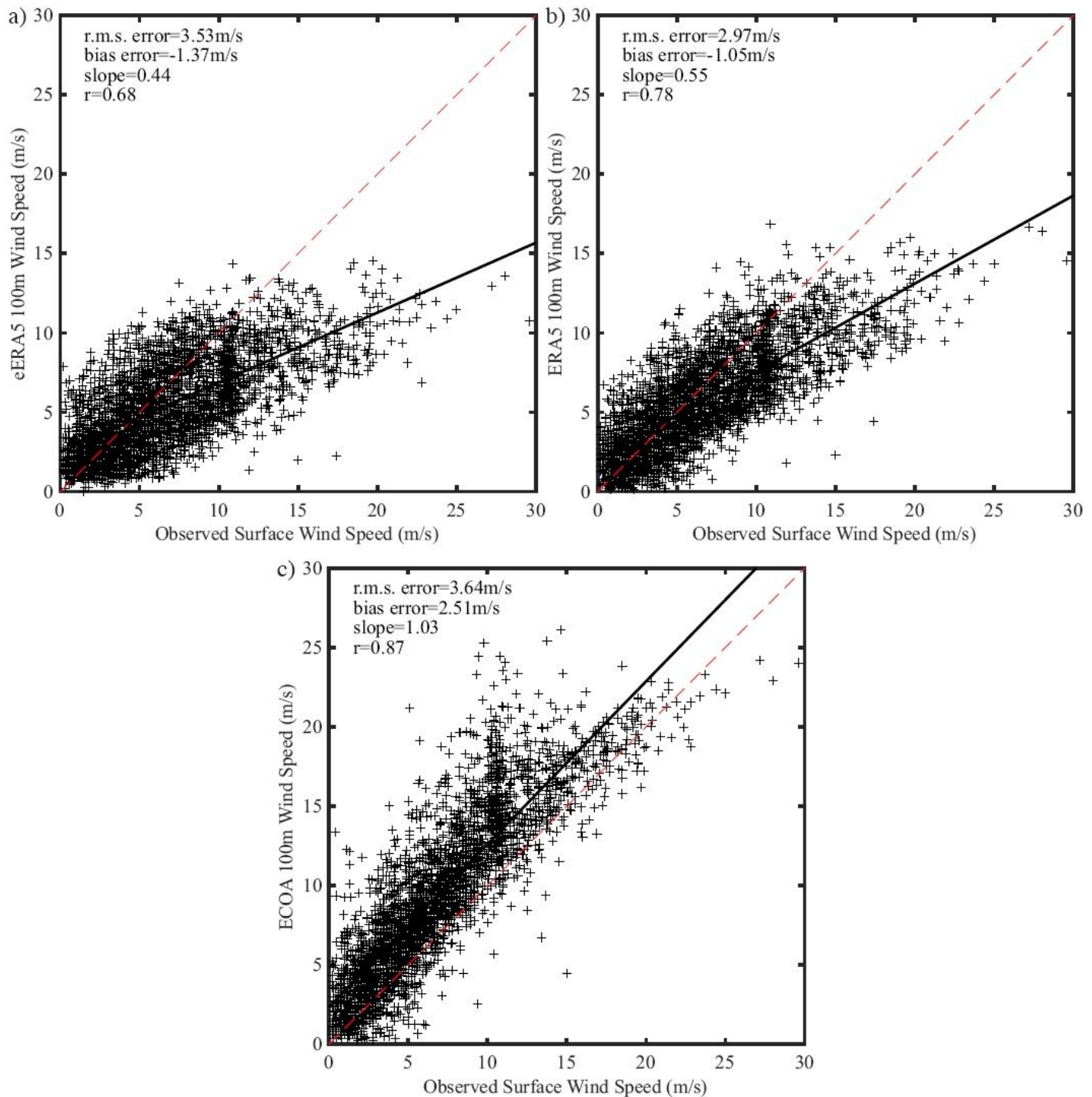


**Figure 5**

Scatterplots of the observed 6-hourly surface wind speed and the 100m model wind speed at Hans Island. Results are shown for: a) the unperturbed member of the ensemble ERA5 reanalysis; b) the ERA5 reanalysis and c) the ECOA. Data from January 1 2016-September 30 2020 excluding May-July 2016 was used.

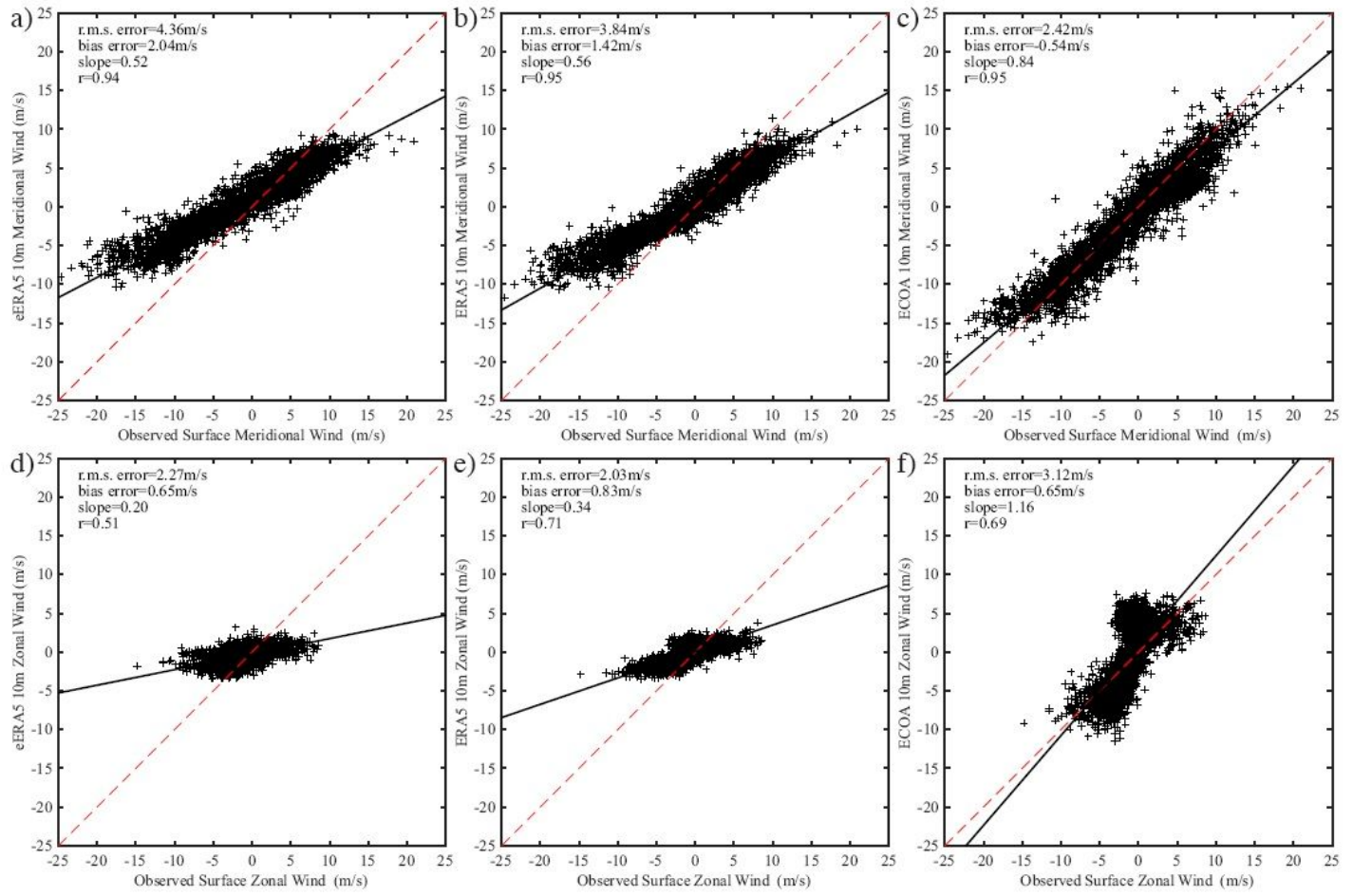


**Figure 6**

Scatterplots of the observed 6-hourly components of the surface wind and the components of the 10m model wind at Hans Island. Results are shown for the meridional component for : a) the unperturbed member of the ensemble ERA5 reanalysis; b) the ERA5 reanalysis and c) the ECOA. Results are also shown for the zonal component for: d) the unperturbed member of the ensemble ERA5 reanalysis; e) the ERA5 reanalysis and f) the ECOA. Data from January 1 2016-September 30 2020 excluding May-July 2016 was used.

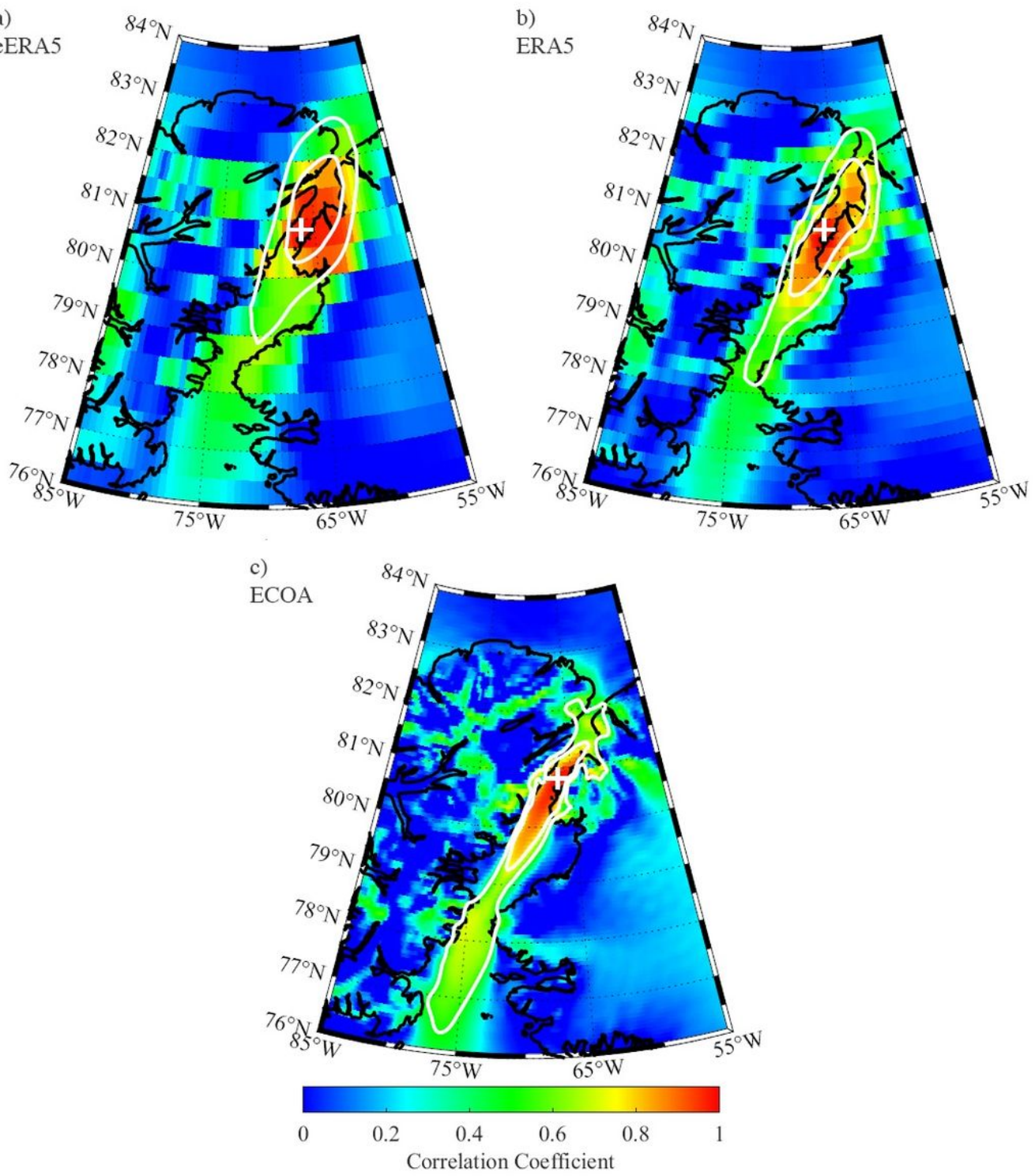


**Figure 7**

One-point correlation maps showing the correlation between the 10m wind speed at Hans Island and at other gridpoints in the Nares Strait region as represented in the : a) eERA5; b)ERA5 and c) ECOA for the period 2016-2020. The location of Hans Island is indicated by the '+'. The 0.5 and 0.7 correlation coefficient contours are shown in white. Note: The designations employed and the presentation of the material on this map do not imply the expression of any opinion whatsoever on the part of Research

Square concerning the legal status of any country, territory, city or area or of its authorities, or concerning the delimitation of its frontiers or boundaries. This map has been provided by the authors.

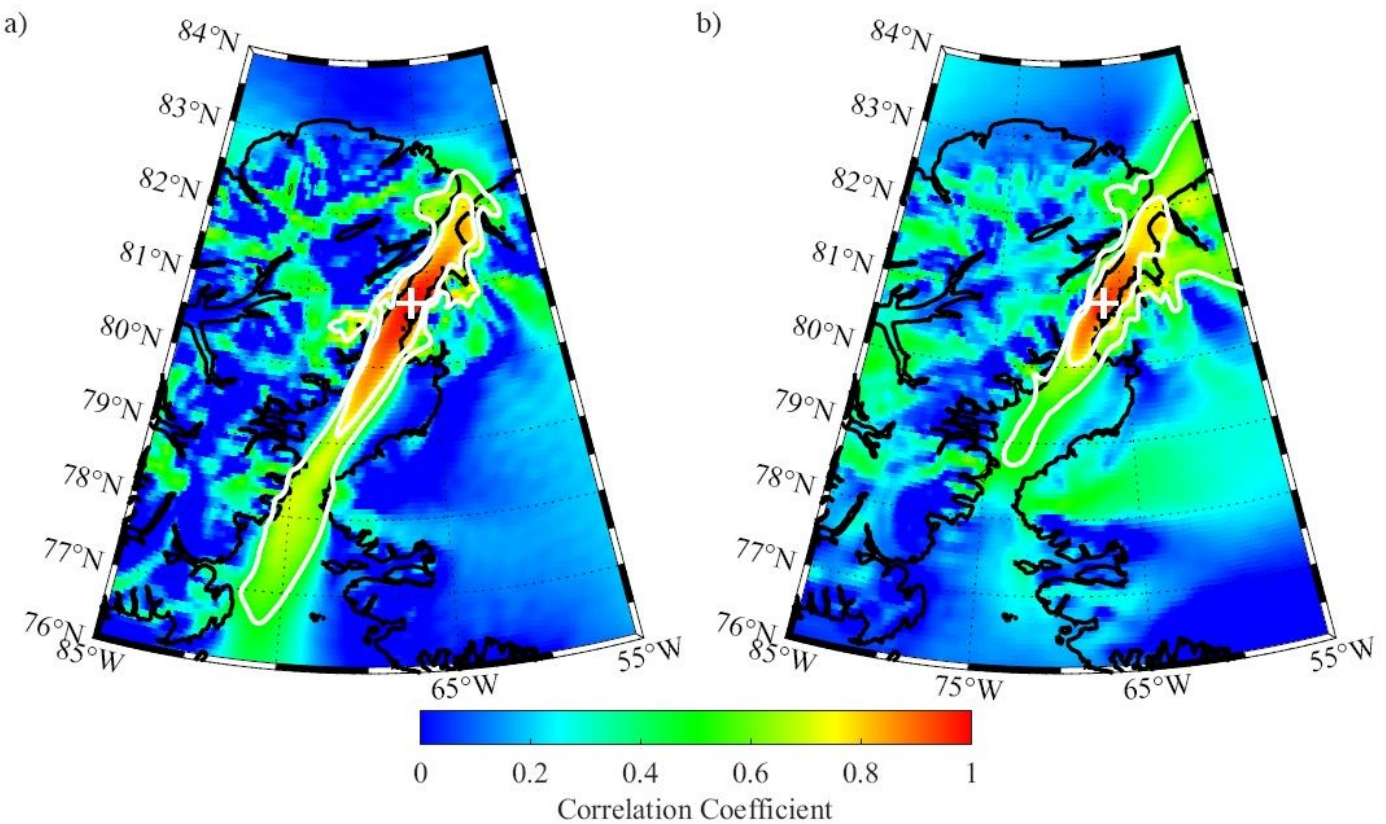


**Figure 8**

One-point correlation maps showing the correlation between the 10m wind speed at Hans Island and at other gridpoints in the Nares Strait region as represented in the ECOA. Results are shown for times during the period 2016-2020 during which there was: a) northerly and b) southerly flow at Hans Island. The location of Hans Island is indicated by the '+'. The 0.5 and 0.7 correlation coefficient contours are shown in white. Note: The designations employed and the presentation of the material on this map do not imply the expression of any opinion whatsoever on the part of Research Square concerning the legal status of any country, territory, city or area or of its authorities, or concerning the delimitation of its frontiers or boundaries. This map has been provided by the authors.